Berry curvature unravelled by the anomalous Nernst effect in Mn_3Ge

Christoph Wuttke,[1,*] Federico Caglieris,[1] Steffen Sykora,[1] Francesco Scaravaggi,[1,2] Anja U. B. Wolter,[1] Kaustuv Manna,[3] Vicky Süss,[3] Chandra Shekhar,[3] Claudia Felser,[3] Bernd Büchner,[1,2,4] and Christian Hess[1,4,†]

[1]*Leibniz-Institute for Solid State and Materials Research, IFW-Dresden, 01069 Dresden, Germany*

[2]*Institut für Festkörperphysik, TU Dresden, 01069 Dresden, Germany*

[3]*Max Planck Institute for Chemical Physics of Solids, 01187 Dresden, Germany*

[4]*Center for Transport and Devices, TU Dresden, 01069 Dresden, Germany*

(Received 4 February 2019; revised manuscript received 22 July 2019; published 5 August 2019)

The discovery of topological quantum materials represents a striking innovation in modern condensed matter physics with remarkable fundamental and technological implications. Their classification has been recently extended to topological Weyl semimetals, i.e., solid-state systems which exhibit the elusive Weyl fermions as low-energy excitations. Here we show that the Nernst effect can be exploited as a sensitive probe for determining key parameters of the Weyl physics, applying it to the noncollinear antiferromagnet Mn_3Ge. This compound exhibits anomalous thermoelectric transport due to enhanced Berry curvature from Weyl points located extremely close to the Fermi level. We establish from our data a direct measure of the Berry curvature at the Fermi level and, using a minimal model of a Weyl semimetal, extract the Weyl point energy and their distance in momentum space.

DOI: 10.1103/PhysRevB.100.085111

I. INTRODUCTION

Weyl semimetals [1–4] are certainly one of the most stunning representatives of topological material classes. Their electronic band structure is predicted to host Weyl points, i.e., three-dimensional linear band crossings that represent massless Weyl fermions of defined chirality. Two Weyl points always form a pair of opposite chirality which is separated in momentum space due to spin-orbit coupling and breaking of the time-reversal symmetry or inversion symmetry. Weyl points act as source or sink of Berry curvature, a vector field in momentum space which represents the topological properties in a material. Understanding, probing, and controlling this quantity is of enormous importance to emergent fields of basic and applied research. For example, in spintronics [5] the Berry curvature is causing a spin-orbit torque that drives spin dynamics in transition-metal bilayers [6]. A further example is quantum computing, where the Berry curvature provides a superior robustness to noise in photonic networks of solid-state qubits [7].

The Berry curvature can be seen as an effective magnetic field in the reciprocal lattice, determining an additional component to the electron velocity $\mathrm{v}(\mathbf{k})$, the so-called anomalous velocity, which is always perpendicular to the force driving the electron motion [8]. As a natural consequence, anomalous transverse transport properties, namely, the anomalous Hall effect (AHE) and its thermoelectric counterpart, the anomalous Nernst effect (ANE), are expected to arise [8–11] and have been measured in several systems [12–14]. The Nernst effect often is dominated by the transverse Peltier coefficient α_{ij}, which probes the electrons only within the energy window determined by the thermal broadening of the Fermi function. The ANE is thus expected to be a more sensitive probe for the Berry curvature at the Fermi level than the AHE which probes the whole Fermi sea [12,15].

Recently the isostructural noncollinear antiferromagnets Mn_3Ge and Mn_3Sn have attracted tremendous interest [5] due to giant anomalous transport coefficients [3,15–19]. Mn_3Sn has been extensively studied in Hall [3] and Nernst measurements [15,17], but it lacks magnetic order below $T = 50\,\mathrm{K}$ and develops a glassy ferromagnetic ground state [20,21], where both ANE and AHE vanish [15]. This is in contrast to Mn_3Ge, where magnetic order and anomalous transport persist down to lowest temperatures, and which is at the focus of this paper. Mn_3Ge is characterized by a hexagonal crystal structure (space group $P6_3/mmc$), where Mn atoms form a kagome lattice of mixed triangles and hexagons with Ge atoms being situated at the center of the hexagons. In the noncollinear antiferromagnetic ground state of Mn_3Ge ($T_N \approx 365$ to $400\,\mathrm{K}$ [22–25]) the Mn moments are oriented at 120° with respect to their neighbors [26] [see Fig. 1(a)]. Only a very small net moment of $\approx 0.02\,\mu_B$ appears in-plane due to a slight tilting of the Mn moments [23,27]. Multiple Weyl points have been predicted to exist in the band structure of Mn_3Ge [26].

Here we report a comprehensive study of the ANE [28] in the noncollinear antiferromagnet Mn_3Ge. We observe at all temperatures studied that the Nernst effect is dominated by a field-saturated anomalous contribution if an in-plane magnetic field $B > 0.02\,\mathrm{T}$ is applied. We derive the anomalous transverse Peltier coefficient from the ANE data and show that its temperature dependence can be analyzed to extract key properties of the Weyl semimetal, i.e., the Weyl point energy, the momentum space separation of two Weyl points, and the effective strength of the Berry curvature at the Fermi level.

In Sec. II we describe the experimental details. In Sec. III we show corresponding experimental results and demonstrate

*c.wuttke@ifw-dresden.de

†c.hess@ifw-dresden.de

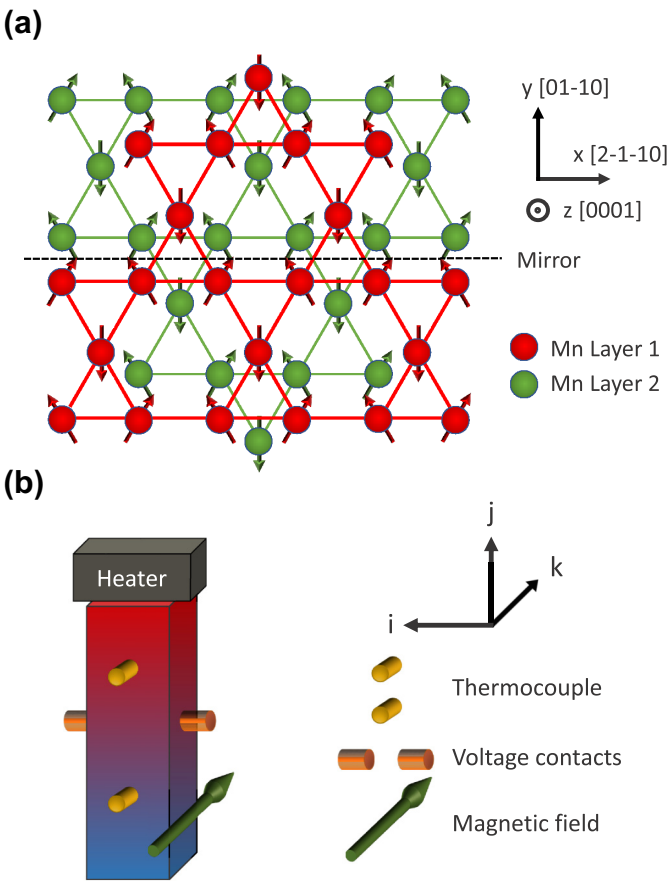

FIG. 1. (a) Mn atoms and magnetic structure of Mn_3Ge. Ge atoms are in the center of each Mn hexagon (not sketched here). By mirroring (xz-mirror plane) and translating by $c/2$ along the z axis the different layers are transformed into each other. (b) Schematic Nernst setup for measuring S_{ij}. On the upper side a resistive chip heater creates the thermal gradient. The bottom of the sample is coupled to a thermal bath of controlled temperature, therefore the temperature gradient arises along the j direction. The magnetic field is applied in the k direction, and the Nernst signal is measured along the i direction.

that the Nernst effect in Mn_3Ge is purely anomalous. Our theoretical model to analyze the temperature dependence of the anomalous Peltier and Hall coefficients is presented in Sec. IV A and furthermore applied to Mn_3Ge where important Weyl point properties are extracted from experimental data. Finally, we discuss and summarize our results in Sec. V and Sec. VI.

II. EXPERIMENTAL

The Mn_3Ge single crystals were grown using the Bridgman-Stockbarger technique. First, the high-purity metals were premelted in an alumina crucible using induction melting. Then the crushed powder was filled in a custom-designed sharp-edged alumina tube and sealed inside a tantalum tube. The crystal growth temperature was controlled using a thermometer at the bottom of the ampule. The sample was heated to 1000 °C, held there for 12 h to ensure homogeneous mixing of the melt, and then slowly cooled to 750 °C. Finally, the sample was quenched to room temperature to retain its high-temperature hexagonal phase. The single crystallinity was checked by white-beam backscattering Laue x-ray diffraction at room temperature. The crystal structures were analyzed with a Bruker D8 VENTURE x-ray diffractometer using Mo-K radiation.

Thermoelectric measurements were done in a home-built probe in a helium cryostat with a magnetic field of up to 15 T. The thermal gradient is generated with a chip resistor on one end of the sample, the other end is glued to a cold bath with an Al_2O_3 plate in between to establish electrical current free conditions. The gradient along the sample is measured with a magnetic-field-calibrated AuFe/Chromel-P thermocouple. The Nernst voltage is measured perpendicular to the thermal gradient and the applied field. The different measurement configurations are labeled as S_{ij}, with the Nernst signal measured along the i direction with an applied temperature gradient ∇T_j and a magnetic field B_k [compare Fig. 1(b)].

Due to its general dependence on the temperature as well as the magnetic field, the Nernst signal is usually measured in two different modes. A temperature-dependent Nernst signal measurement contains two separate temperature sweeps. During the first sweep the magnetic field is fixed to a certain field, and the second sweep is measured at the corresponding inverted magnetic field (in this work $B = 14$ T and $B = -14$ T). Afterwards the data are antisymmetrized to get rid of any contribution of the Seebeck effect caused by slightly misaligned contacts. A magnetic-field-dependent measurement is conducted at a fixed temperature while sweeping the magnetic field from negative to positive values or vice versa. This was not possible for the magnetic-field-dependent measurements in Mn_3Ge, due to the peculiar hysteretic behavior at small fields, which leads to different $S_{ij}(B)$ curves depending on the field history. Therefore, the Nernst signal was measured in full field cycles, from $B = -15$ T to $+15$ T and back to -15 T. By subtraction of the symmetric contribution (which shows no field dependence), the curves were centered around $S_{ij}(B) = 0$ to allow a comparison of different temperatures.

III. NERNST EFFECT RESULTS

We start with a clear demonstration that the anomalous transport (which is driven by Berry curvature) dominates the Nernst effect in Mn_3Ge. Figure 2(a) shows the Nernst coefficient S_{xz} which exhibits a totally anomalous behavior (no magnetic field dependence) without any visible normal (linear B dependence) contribution as a function of field for all the investigated temperatures, exhibiting a steplike feature at very low fields and reaching a saturation in a flat plateau for $B > 0.02$ T (the distinct steplike behavior at $B < 0.02$ T as well as the relation between Nernst data and magnetization are discussed in detail in Appendix C). S_{yz} reveals a very similar field dependence as presented in Fig. 2(b). Both configurations show the peculiar saturating behavior up to room temperature with a large Nernst signal of around $0.4-1.5$ μV/K, depending on the temperature. On the other hand, a different phenomenology characterizes S_{xy}, as reported in Fig. 2(c). In this configuration the Nernst coefficient is much smaller, with the steplike behavior just slightly visible, and shows a much weaker temperature dependence.

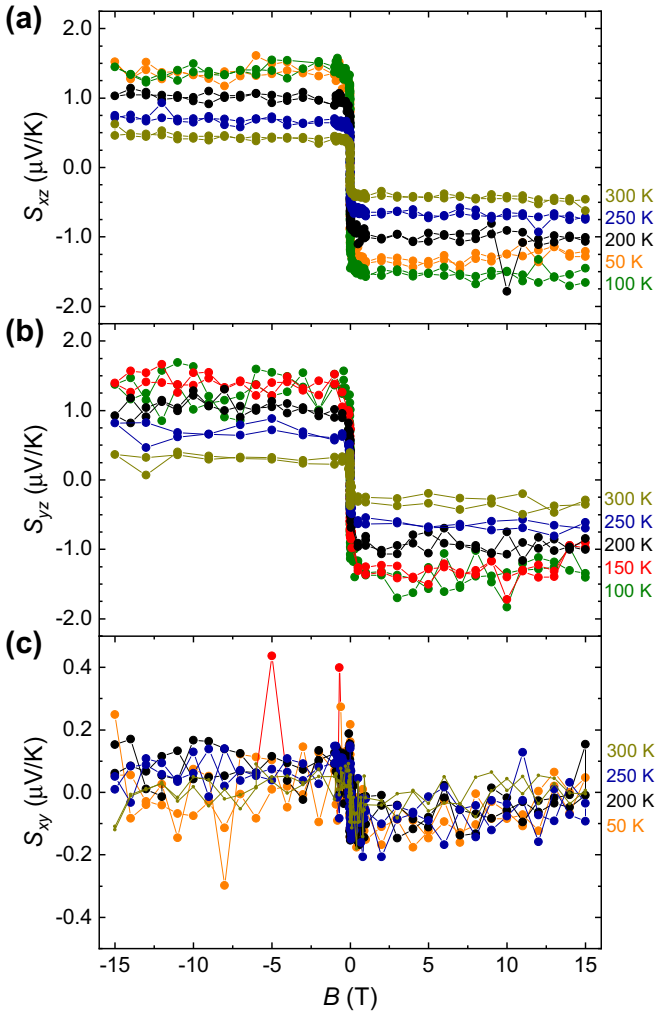

FIG. 2. (a)–(c) Nernst signal of the Mn_3Ge single crystals with respect to the applied magnetic field B in different configurations. S_{ij} is obtained by measuring the voltage along the i direction while applying a thermal gradient ∇T and a magnetic field B along the j and k directions, respectively.

The experimental observation in Fig. 2(a) allows us to draw an important conclusion about the Berry curvature in Mn_3Ge. The Nernst signal S_{xz} of the transverse transport is generally determined by the thermoelectric tensor α and the charge conductivity tensor σ as

$$S_{xz} = \frac{\alpha_{xz}\sigma_{xx} - \alpha_{xx}\sigma_{xz}}{\sigma_{xx}^2 + \sigma_{xz}^2}, \tag{1}$$

where each transverse transport coefficient ($S_{xz}, \alpha_{xz}, \sigma_{xz}$) is the sum of a normal and an anomalous contribution. The observed saturation in the Nernst signal without any field dependence at $B > 0.02$ T is incompatible with normal transport [12,17] and thus implies that all normal contributions are negligible in S_{xz}. Hence, in what follows we solely consider only anomalous transport coefficients α_{xz} and σ_{xz} for analyzing our data. It is well established that the anomalous Peltier and Hall coefficients α_{xz} and σ_{xz} are related to the y component of the momentum-integrated Berry curvature $\mathbf{\Omega} = (\Omega^x, \Omega^y, \Omega^x)$ via the expressions

$$\sigma_{xz} = \frac{e^2}{\hbar}\int \frac{d^3k}{(2\pi)^3}\Omega^y(\mathbf{k})f_{\mathbf{k}}, \tag{2}$$

$$\alpha_{xz} = \frac{k_B e}{\hbar}\int \frac{d^3k}{(2\pi)^3}\Omega^y(\mathbf{k})s_{\mathbf{k}}, \tag{3}$$

where $f_{\mathbf{k}}$ is the Fermi distribution function and $s_{\mathbf{k}}$ is the entropy density [29]. Thus, if a large anomalous Nernst signal S_{xz} is observed, the y component of the integrated Berry curvature must be large too. The almost identical observation for S_{yz} [see Fig. 2(b)] implies the same statement for Ω^x. Since S_{xy} exhibits only a suppressed value without any clear anomalous contribution, these considerations allow us to conclude that the integrations of the x and y components of the Berry curvature are large compared to its integrated z component, caused by an either vanishing or odd Ω^z with respect to $k_z = 0$ [$\Omega^z(k_x, k_y, k_z) = -\Omega^z(k_x, k_y, -k_z)$]. These findings are consistent with symmetry considerations of the band structure [24,26], according to which Ω^z is an odd function in k_z, whereas Ω^x is even in k_x if the magnetic field is applied along x and likewise for Ω^y.

The saturation values of S_{xz}, S_{yz}, and S_{xy} at $B = 14$ T are plotted in Fig. 3(a) as a function of temperature T. A broad maximum of about 1.5 μV/K is visible for S_{xz} and S_{yz} at around 100 K, whereas S_{xy} is negligibly small. This remarkable temperature dependence is leading us to a second qualitative fundamental conclusion. As is explained in Ref. [12], the peak position in the temperature dependence of the ANE represents a coarse correspondence with the lowest Weyl point energy μ with respect to the Fermi level. This is because for $k_BT \ll |\mu|$ essentially states with energy $|\epsilon| < |\mu|$ probe the Berry curvature and contribute to the ANE, giving rise to an increase of it upon the thermal energy approaching $|\mu|$ from below. On the other hand, if k_BT becomes comparable with $|\mu|$ or even exceeds it, the then additionally contributing higher energy states at $|\epsilon| > |\mu|$ provide an opposite contribution to the ANE. Thus, we estimate $|\mu| \sim 10$ meV. It has been suggested that in Mn_3Ge the presence of spin-orbit coupling removes the degeneracy at the Weyl point and leads to an opening of a gap [31]. In this case the energy $|\mu|$ remains meaningful and describes the distance between the center of the gap and the Fermi level.

After having established a qualitative understanding of the ANE, we now move on to extract material-specific parameters of the Weyl system. In order to provide a quantitative evaluation we derived the transverse Peltier coefficient

$$\alpha_{xz} = \frac{\rho_{zz}S_{xz} - \rho_{xz}S_{zz}}{\rho_{xx}\rho_{zz} + \rho_{xz}^2} \tag{4}$$

using experimental values for the required transport coefficients (see Appendix A). The temperature dependence of α_{xz} in zero field is shown in Fig. 3(b). It resembles the behavior of S_{xz} but exhibits a narrower maximum which is shifted to lower temperatures (≈ 75 K). It is worth noting that indeed the anomalous Nernst signal dominates α_{xz}. This can be inferred from Fig. 3(c) where the two contributions $\rho_{zz}S_{xz}/(\rho_{xx}\rho_{zz} + \rho_{xz}^2)$ and $-\rho_{xz}S_{zz}/(\rho_{xx}\rho_{zz} + \rho_{xz}^2)$ are directly compared. Thus α_{xz} is truly anomalous as well and is given by Eq. (3). We

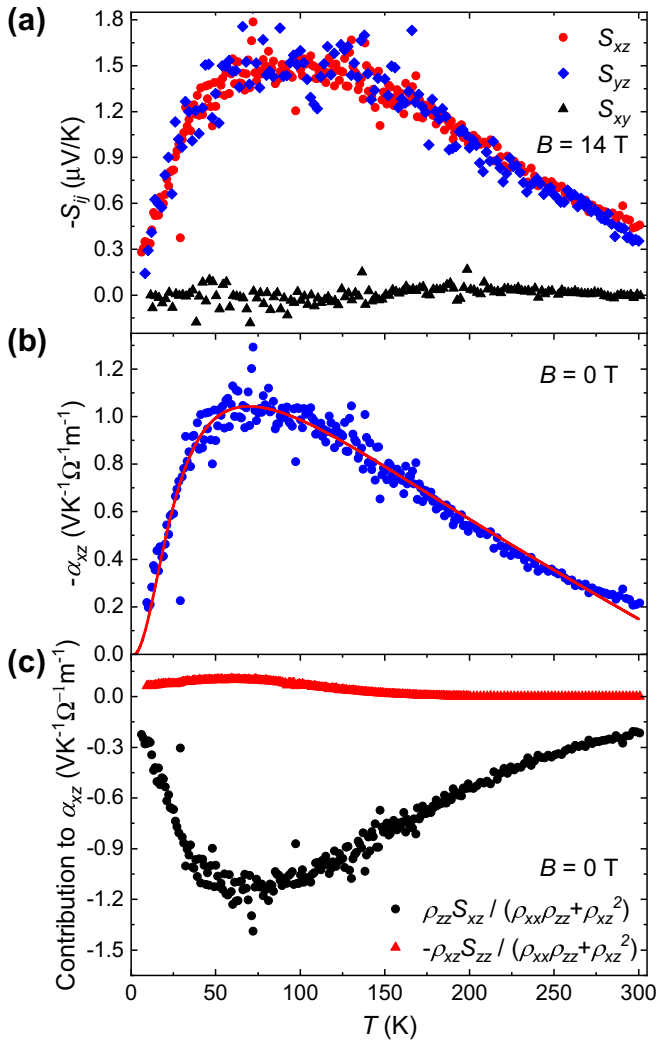

FIG. 3. Temperature dependence of (a) S_{ij} at $B = 14$ T, (b) α_{xz} obtained by using the relation $\alpha_{xz} = (\rho_{zz}S_{xz} - \rho_{xz}S_{zz})/(\rho_{xx}\rho_{zz} + \rho_{xz}^2)$ [30] (blue dots) and the fit provided by our theoretical model (red line); (c) the two terms contributing to α_{xz}.

use this as a starting point to develop a model to analyze the temperature dependence of α_{xz} in more detail and to extract important Weyl point properties from our experimental result of Fig. 3(b).

IV. THEORETICAL MODELING AND DATA ANALYSIS

A. Model

Extending the theory proposed in Ref. [12] we start from a generalized expression of Eq. (3) for a multiband system,

$$\alpha_{xz} = \frac{e^2}{\hbar}\sum_n \int \frac{d^3k}{(2\pi)^3}\Omega_n^y(\mathbf{k})s_{n,\mathbf{k}}, \tag{5}$$

where $s_{n,\mathbf{k}} = -f_{n,\mathbf{k}}\ln f_{n,\mathbf{k}} - [(1-f_{n,\mathbf{k}})\ln(1-f_{n,\mathbf{k}})]$ is the entropy density [$f_{n,\mathbf{k}} = f(E_{n\mathbf{k}})$: Fermi distribution function] for the dispersion $E_{n,\mathbf{k}}$ of the conduction electron band n. We assume that this anomalous contribution is predominantly determined by one particular pair of Weyl nodes which are

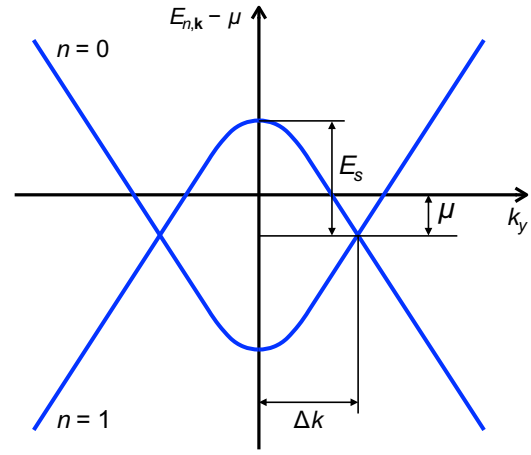

FIG. 4. Schematic picture of the band dispersion in a Weyl semimetal. The Weyl points of opposite chirality are placed along the k_y direction. Saddle point energy, energy of the Weyl points with respect to the Fermi level, and their distance from $k_y = 0$ are labeled as E_S, μ, and Δk, respectively.

placed extremely close to the Fermi level [26]. The vector $\mathbf{\Omega}_n(\mathbf{k})$ is the Berry curvature with respect to the band n. We consider two bands which are separated in energy and which touch each other in the pair of Weyl nodes (compare Fig. 4). They are indexed by $n = 0$ (high-energy band with $E_{0,\mathbf{k}} > 0$) and $n = 1$ (low-energy band with $E_{1,\mathbf{k}} < 0$). For the dispersion we apply the following minimal model [32] of linearized Weyl fermions,

$$E_{n,\mathbf{k}} = \pm v_F\sqrt{k_x^2 + (k_y \pm \Delta k)^2 + k_z^2}. \tag{6}$$

It describes a pair of Weyl points which are placed at energy $E = 0$ and are separated in momentum space by $2\Delta k$.

We replace at first the momentum integral in Eq. (5) with an energy integral,

$$\alpha_{xz} = \frac{e^2}{\hbar}\int_{-\infty}^{0} dE\,\rho_1(E)\Omega_1^y(E)s(E) + \frac{e^2}{\hbar}\int_0^{\infty} dE\,\rho_0(E)\Omega_0^y(E)s(E), \tag{7}$$

where $\rho_n(E)$ is the density of states with respect to the band "n." For the linearized band structure (6) the density of states is given by

$$\rho_0(E) = \begin{cases} 0 & : \quad E < 0 \\ \rho_0 E^2 & : \quad 0 \leqslant E \leqslant E_s \\ \frac{\rho_0}{2}E(E_s + E) & : \quad E > E_s \end{cases}, \tag{8}$$

$$\rho_1(E) = \begin{cases} 0 & : \quad E > 0 \\ \rho_0 E^2 & : \quad -E_s \leqslant E \leqslant 0 \\ \frac{\rho_0}{2}E(-E_s + E) & : \quad E < -E_s \end{cases}, \tag{9}$$

where ρ_0 is a constant in energy and $E_s = v_F\Delta k$ is the energy difference between the Weyl point and the saddle point at $\mathbf{k} = 0$ (compare Fig. 4). Note that the total density of states $\rho = \rho_0 + \rho_1$ is symmetrical around the Weyl point, i.e., $\rho(-E) = \rho(E)$, and it vanishes at the Weyl points $E = 0$. The explicit formula for the energy dependence of the entropy density $s(E)$

in Eq. (7) reads

$$s(E) = \frac{\ln(1+e^{\beta(E-\mu)})}{1+e^{\beta(E-\mu)}} + \frac{\ln(1+e^{-\beta(E-\mu)})}{1+e^{-\beta(E-\mu)}}, \tag{10}$$

where μ is the chemical potential and $\beta = 1/(k_B T)$ the inverse temperature. Note that the chemical potential might also be temperature-dependent.

The vector of the Berry curvature in Eqs. (5) and (7) can be obtained by a standard linear response theory as introduced by Kubo [33]. The general formula for the vector of the Berry curvature in a multiband system reads

$$\mathbf{\Omega}_n(\mathbf{k}) = i\hbar^2 \sum_{m\neq n} \frac{\langle\psi_{n,\mathbf{k}}|\hat{\mathbf{v}}|\psi_{m,\mathbf{k}}\rangle \times \langle\psi_{m,\mathbf{k}}|\hat{\mathbf{v}}|\psi_{n,\mathbf{k}}\rangle}{(E_{n,\mathbf{k}} - E_{m,\mathbf{k}})^2}, \tag{11}$$

where $|\psi_{n,\mathbf{k}}\rangle$ are the Bloch states and $\hat{\mathbf{v}}$ is the velocity operator. Within our linearized model we neglect the energy dependence of the velocity matrix elements and assume that the Berry curvature is equal for the two bands. Thus, the energy dependence of one component of $\mathbf{\Omega}_n$ is determined by the quadratic energy denominator in the Kubo formula (11). Hence, we set for the y component

$$\Omega_0^y(E) = \Omega_1^y(E) = \frac{\hbar^2\tilde{\Omega}}{4E^2}, \tag{12}$$

with an open parameter $\tilde{\Omega}$ representing the off-diagonal velocity matrix elements in Eq. (11) in a field which breaks the time-reversal symmetry of the system. Note that the Berry curvature diverges at the Weyl point energy $E = 0$.

Inserting the expressions (8), (9), and (12) in the formula (7) for α_{xz} we obtain

$$\alpha_{xz} = \frac{e^2\hbar\tilde{\Omega}\rho_0}{4}\left[\int_{-E_s}^{E_s} s(E)\,dE + \frac{1}{2}\int_{-\infty}^{-E_s} \frac{-E_s+E}{E} s(E)\,dE + \frac{1}{2}\int_{E_s}^{\infty} \frac{E_s+E}{E} s(E)\,dE\right], \tag{13}$$

where for $s(E)$ the expression (10) (considering μ and β as constant in energy) has to be used. To simplify the solution of the integrals with the aim of obtaining a fitting formula for the temperature dependence we substitute at first the variable E with the Fermi distribution function $F(E) = 1/(1+e^{\beta E})$. Exploiting the property that $F(E)$ can take values only between 0 and 1 we then perform a Taylor expansion in terms of F around the value 1/2 up to the first order in $(F - 1/2)$. Due to the exponential functions in $s(E)$ the power series of F converges quickly if the temperature is not too large. After this expansion we integrate over F and obtain the following result:

$$\begin{aligned}\alpha_{xz} = C_\alpha k_B T \Bigg\{ & 1 - \frac{E_s}{\mu} - \frac{E_s k_B T}{\mu^2} \\ & + F(-E_s-\mu)\left(1 + \frac{E_s}{\mu} - 2\frac{E_s k_B T}{\mu^2}\right) \\ & + F(E_s-\mu)\left(-1 + \frac{E_s}{\mu} - 2\frac{E_s k_B T}{\mu^2}\right) \\ & + 2\frac{E_s k_B T}{\mu^2}[F^2(E_s-\mu) - F^2(-E_s-\mu)]\Bigg\},\end{aligned} \tag{14}$$

with $F(E) = 1/(1+e^{\beta E})$ and $C_\alpha = (e^2\hbar\tilde{\Omega}\rho_0 \ln 2)/2$. Note that the chemical potential μ, which is derived below, is in general temperature-dependent, i.e., $\mu = \mu(T)$. After inserting this function $\mu(T)$ into Eq. (14) we obtain the desired fitting formula for the temperature dependence of the Peltier coefficient α_{xz}.

As can be seen in Eq. (14), the parameter C_α plays a specific role which is used in our analysis. $C_\alpha = (e^2\hbar\tilde{\Omega}\rho_0 \ln 2)/2$, where $\tilde{\Omega}$ is according to Eqs. (11) and (12) a parameter which characterizes the off-diagonal velocity matrix elements of the Berry curvature. ρ_0 is defined in Eqs. (8) and (9) and represents the amplitude of the density of states which is mainly determined by the band dispersion.

Let us finally derive an approximate expression for $\mu(T)$. Generally, this function can be found from the relation between the total particle number and the chemical potential which is given by an integral over the Fermi distribution as

$$N = \int_{-\infty}^{\infty} F(E-\mu)\rho(E)\,dE, \tag{15}$$

where $\rho(E) = \rho_0(E) + \rho_1(E)$ is the total density of states with the two parts ρ_0 and ρ_1 as given by Eqs. (8) and (9). Evaluating the energy integral in Eq. (15) and then solving the resulting expression for μ gives rise to the function $\mu = \mu(N,T)$. Unfortunately, the exact solution can only be found numerically. To find an approximate analytical formula for $\mu(T)$ we simplify the integration in Eq. (15) by replacing the exponential behavior of the Fermi distribution function $F(E-\mu)$ around $E = \mu$ with a linear function in E. More specifically, we model the function $F(E-\mu)$ to linearly drop to zero in the energy range $k_B T$ around $E = \mu$. For E values below and above this range we set F equal to 1 and 0, respectively. Such an approximation is valid if the temperature is not too large ($k_B T < 2E_s$). We obtain from Eq. (15)

$$\begin{aligned} N \approx & \int_{-\infty}^{-E_s} \frac{\rho_0}{2} E(-E_s+E)\,dE \\ & + \int_{-E_s}^{\mu-\frac{k_B T}{2}} \rho_0 E^2 dE + \rho_0\mu^2\frac{k_B T}{2}. \end{aligned} \tag{16}$$

Forming the derivative with respect to $(k_B T)$ on both sides of Eq. (16) leads to the following approximate differential equation for the chemical potential:

$$0 \approx \mu^2\mu' + \mu\frac{k_B T}{2} + \left(\frac{k_B T}{2}\right)^2\left(\mu' - \frac{1}{2}\right). \tag{17}$$

At zero temperature $T = 0$ we immediately find $\mu' = 0$. In the high-temperature limit $\mu \ll k_B T$, Eq. (17) suggests a linear behavior of μ with temperature, i.e., $\mu \propto k_B T$. Therefore, we assume the following approximate temperature behavior:

$$\mu(T) \approx \sqrt{\mu_0^2 + (Ak_B T)^2}, \tag{18}$$

where μ_0 is the chemical potential at zero-temperature, i.e., $\mu_0 = \mu(T=0)$. This ansatz fulfills the above properties as one can easily verify by considering the corresponding limiting cases. According to Fig. 4, μ_0 defines the energy of

the Weyl point relative to the Fermi level. The dimensionless constant A can be obtained by inserting the ansatz (18) into the differential Eq. (17) in the limit $k_B T \ll \mu$. We find the following equation for A,

$$A^3 + \frac{3}{4}A - \frac{1}{8} \approx 0, \tag{19}$$

which has the solution $A \approx 0.162$. Note that this constant determines the change of the chemical potential with temperature in the high-energy regime. Therefore, in the real multiband material where several Weyl points are present we expect for A a value larger than 0.162. Qualitatively, A is a measure for degrees of freedom of the electronic system at the Fermi level. In the case of trivial bands being absent it roughly corresponds to the number of high-energy Weyl points in the material times the number 0.162. Therefore we can slightly modify Eq. (18), using the quantity of N_W instead of A,

$$\mu(T) \approx \sqrt{\mu_0^2 + (0.162 N_W k_B T)^2}. \tag{20}$$

In summary, the expression (14) together with Eq. (18) provides a fitting formula for the temperature dependence of the Peltier coefficient α_{xz}. The fitting parameters are A, C_α, μ_0, and E_S. The saddle point energy $E_S = v_F \Delta k$ is related to the separation of the Weyl points of opposite chirality in momentum space, and μ_0 describes the energy difference between the Weyl point and the Fermi level at $T = 0$. Note that μ_0 is usually considered in band structure calculations as the Weyl point energy and is therefore of particular interest. Within our model the values E_s and μ_0 are assigned to the particular low-energy Weyl point which arises from the crossing of our two linearized bands. These energy values are related to the Weyl point with the lowest possible energy.

The remaining parameter $C_\alpha = (e^2 \hbar \tilde{\Omega} \rho_0 \ln 2)/2$ is a constant which represents the order of magnitude of α_{xz}, directly proportional to the amplitude of the density of states ρ_0 and the experimentally relevant strength of the Berry curvature of the considered Weyl system near the Fermi level, $\tilde{\Omega}$.

B. Analysis of Mn_3Ge data

In order to extract the important geometric properties of the underlying system of Weyl fermions close to the Fermi level, we fit the experimental data [red line in Fig. 3(b)] using the formula (14). As can be seen clearly, the fit works well in a wide temperature range. The deviation at high temperature above 250 K can be explained within the approximation made to derive Eq. (14). The obtained parameter $\mu_0 = 6.6 \pm 0.7$ meV is remarkably close to 8 meV, the energy of the particular Weyl point W_4 provided by band structure calculations [26] of Mn_3Ge. From the saddle point energy $E_s = 90 \pm 25$ meV and $v_F \approx 1\,\mathrm{eV}/\pi$ [26] we calculate a momentum space separation $\Delta k \approx 0.09\,\pi$ using $E_s = v_F \Delta k$. Both this result and estimated total number of Weyl points $N_W = 17.8 \pm 2.2$ also agree well with band structure calculations [26]. Furthermore, while the above parameters determine the momentum space properties, the parameter $C_\alpha = 0.030 \pm 0.002\,\mathrm{V(K\,\Omega\,m)^{-1}}$ contains the materials specific information on the Berry curvature at the Fermi level.

We mention that the anomalous Hall coefficient can be analyzed using a similar approach. However, since an additional approximation is needed for deriving an analytical expression for the AHE, the accuracy of such an analysis of σ_{xz} is comparably lower (see Appendix B for details).

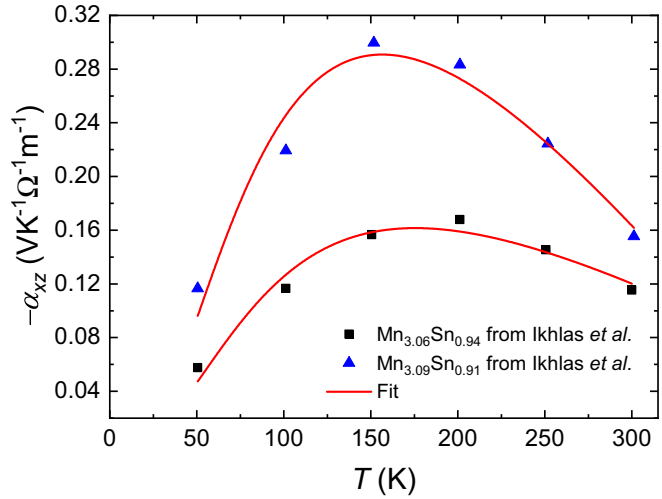

FIG. 5. α_{xz} in $Mn_{3.06}Sn_{0.94}$ (black squares) and $Mn_{3.09}Sn_{0.91}$ (blue triangles) from Ref. [17]. The corresponding fits of the data are represented by red lines. We extracted values of $\mu_0 = 45$ meV, $C_\alpha = 0.004\,\mathrm{V(K\,\Omega\,m)^{-1}}$ for $Mn_{3.06}Sn_{0.94}$ and $\mu_0 = 108$ meV, $C_\alpha = 0.010\,\mathrm{V(K\,\Omega\,m)^{-1}}$ for $Mn_{3.09}Sn_{0.91}$.

V. DISCUSSION

Our findings show clearly that the anomalous Nernst effect, beyond the mere statement that the integrated Berry curvature near the Fermi level is finite for a given material, can also be used as a sensitive probe for the experimentally relevant strength of the Berry curvature. In this regard it is interesting to compare the obtained quantities with other Weyl materials exhibiting a similar density of states ρ_0. For this purpose, we performed an analogous analysis of existing transport data [17] of the isostructural Weyl compound Mn_3Sn; see Fig. 5. At $T = 300$ K, S_{xz} and S_{yz} exhibit exactly the same steplike behavior as our data. Interestingly, α_{xz} in Mn_3Sn is one order of magnitude smaller than in Mn_3Ge. Thus, the Berry curvature in Mn_3Sn at the Fermi level is significantly smaller than in Mn_3Ge, since both materials possess a similar density of states ρ_0 [26]. This difference is consistent with theoretical results in Ref. [34]. Furthermore, the peak of α_{xz}, compared to Mn_3Ge, is shifted to much higher temperatures. This implies, according to our considerations above, a significantly higher Weyl point energy in Mn_3Sn.

The results of our analysis are shown in Fig. 5, where we have applied Eq. (14) to fit the temperature dependence of α_{xz} in Mn_3Sn. The parameter $C_\alpha = 0.004 \ldots 0.010\,\mathrm{V(K\,\Omega\,m)^{-1}}$, which is nearly an order of magnitude lower than the corresponding value in Mn_3Ge. Furthermore we obtain an energy of the lowest-lying Weyl points in the range of $\mu_0 \approx 40 \ldots 100$ meV, which corresponds well to the value of $\mu = 86$ meV for Mn_3Sn given by band structure calculations in Ref. [26]. These findings correspond to our qualitative comparison of the magnitude and position of the maximum of $\alpha_{xz}(T)$.

The above comparison between Mn_3Ge and Mn_3Sn demonstrates the universal applicability of our analysis to topological materials, and thus allow us to use the ANE for quantitative determination of Weyl point properties.

VI. SUMMARY

In summary, we measured the anomalous Nernst effect in Mn_3Ge and developed a theoretical model to obtain quantitative information on the Weyl nodes in this material. Our analysis reveals an access to fundamental properties of Weyl systems through anomalous transverse transport. On the one hand, the anomalous Nernst effect can be used to determine the Weyl point energy as well as the momentum separation of the lowest-lying Weyl points of the system. On the other hand, and most importantly, our analysis yields a measure of the Berry curvature strength at the Fermi level, which is, to the best of our knowledge, not accessible through other experimental probes. In this way, our study promotes the anomalous Nernst effect as an exceptional bulk probe to detect and study Weyl physics in solid-state materials.

ACKNOWLEDGMENTS

This project has been supported by the Deutsche Forschungsgemeinschaft through project C07 of SFB 1143 (project ID 247310070) and priority program DFG-GRK1621. This project has received funding from the European Research Council (ERC) under the European Unions' Horizon 2020 research and innovation program (grant agreement No 647276-MARS-ERC-2014-CoG).

APPENDIX A: PELTIER COEFFICIENT AND ITS COMPONENTS

Since the Hall effect as well as the Nernst effect show an anomalous behavior, α_{xz} can be calculated using zero field values of all involved transport coefficients. The Peltier tensor

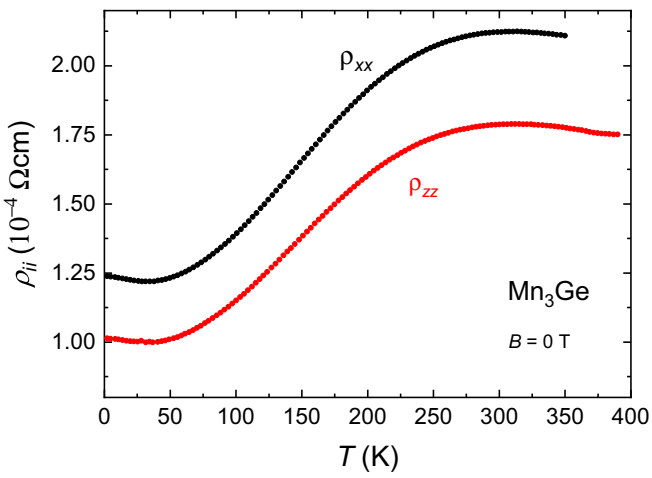

FIG. 6. Temperature-dependent resistivity along the x and z directions.

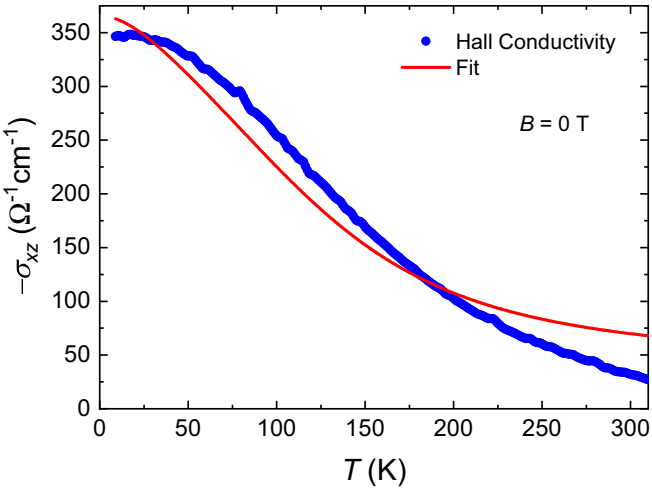

FIG. 7. Plot of the Hall conductivity σ_{xz} vs temperature. Blue dots represent experimental data. The data were fitted (red line) by using our theoretical approach as well as the fixed parameters ($\mu_0 = 8.3$ meV, $E_s = 143$ meV, and $N_W = 22.3$) extracted from the fit of α_{xz}.

$\bar{\alpha}$ can be written as

$$\bar{\alpha} = \bar{\sigma}\bar{S} \tag{A1}$$

with the conductivity tensor $\bar{\sigma}$ and the thermoelectric tensor $\bar{S}$, the former describing longitudinal and Hall conductivities and the latter Seebeck and Nernst coefficients. Focusing on the xz plane, the conductivity tensor can be expressed as the inverse of the resistivity tensor

$$\bar{\sigma} = \bar{\rho}^{-1} = \frac{1}{\det\bar{\rho}}\begin{pmatrix} \rho_{zz} & -\rho_{xz} \\ -\rho_{zx} & \rho_{xx} \end{pmatrix}, \tag{A2}$$

leading to the following form of $\bar{\alpha}$:

$$\bar{\alpha} = \begin{pmatrix} \alpha_{xx} & \alpha_{xz} \\ \alpha_{zx} & \alpha_{zz} \end{pmatrix} = \frac{1}{\rho_{xx}\rho_{zz} - \rho_{xz}\rho_{zx}} \times \begin{pmatrix} \rho_{zz}S_{xx} - \rho_{xz}S_{zx} & \rho_{zz}S_{xz} - \rho_{xz}S_{zz} \\ \rho_{xx}S_{zx} - \rho_{zx}S_{xx} & \rho_{xx}S_{zz} - \rho_{zx}S_{xz} \end{pmatrix}. \tag{A3}$$

With this, one can easily express α_{xz} as

$$\alpha_{xz} = \frac{\rho_{zz}S_{xz} - \rho_{xz}S_{zz}}{\rho_{xx}\rho_{zz} - \rho_{xz}\rho_{zx}}, \tag{A4}$$

or, using the relation $\rho_{xz} = -\rho_{zx}$, as

$$\alpha_{xz} = \frac{\rho_{zz}S_{xz} - \rho_{xz}S_{zz}}{\rho_{xx}\rho_{zz} + \rho_{xz}^2}. \tag{A5}$$

Electrical transport measurements were done in different configurations to calculate the Peltier coefficient α_{xz}. The temperature-dependent resistivity for in-plane and out-of-plane configurations is shown in Fig. 6. Figure 7 shows the xz component of the Hall conductivity. Both quantities are in good agreement with previous measurements [16].

The Seebeck effect was measured using the Nernst setup with one additional electrical contact. The Seebeck coefficient

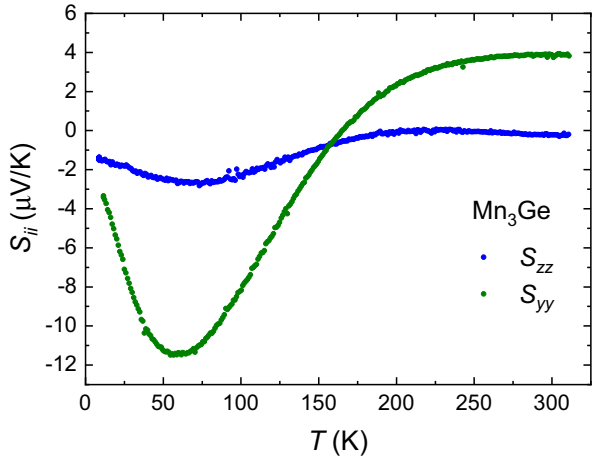

FIG. 8. Temperature-dependent Seebeck coefficient measurement along the y and z directions.

S_{ii} along the y and z axes has been studied. The data are shown in Fig. 8.

APPENDIX B: FITTING OF HALL EFFECT DATA

Using the same arguments as described in Sec. IV A we have derived a similar fitting formula for the anomalous Hall coefficient σ_{xz}, based on the usual expression

$$\sigma_{xz} = \frac{e^2}{\hbar}\int \frac{d^3k}{(2\pi)^3}\Omega^y(\mathbf{k})F(\varepsilon_\mathbf{k}) \tag{B1}$$

as obtained from the Boltzmann transport theory. The evaluation of the momentum integration results in the following formula:

$$\sigma_{xz} = C_\sigma k_B T[2\ln(1+e^{(E_s/2-\mu)/k_BT}) - \ln(1+e^{(-E_s/2-\mu)/k_BT})], \tag{B2}$$

where C_σ is a specific fitting parameter of σ_{xz}. This formula can be used, together with the parameters obtained by fitting the temperature dependence of α_{xz} ($\mu_0 = 6.6 \pm 0.7$ meV, $E_S = 90 \pm 25$ meV, and $N_W = 17.8 \pm 2.2$), to fit the Hall conductivity σ_{xz}. The parameters μ_0, E_S, and N_W were allowed to vary inside the corresponding error bar. The result is displayed in Fig. 7, the remaining parameter $C_\sigma = -3.6 \pm 0.3\,(\Omega\,\mathrm{cm\,meV})^{-1}$. As one can see, the fit works less well than for the Peltier coefficient in Fig. 3(b) for the following reason. Due to the presence of the Fermi function the momentum integration in Eq. (B2) is not restricted to states close to the Fermi level. Therefore, an additional approximation is needed to be included to perform the momentum integration analytically. More specifically, due to the entropy density in the momentum integral of the anomalous Peltier coefficient (at low temperature) it is solely determined by states close to the Fermi level. This is, however, not the case for the anomalous Hall conductivity where states deep in the occupied region of the Fermi sea also contribute. We emphasize at this point that such an additional approximation rather affects the temperature dependence than the overall magnitude. Therefore we believe that the coefficients C_α and C_σ, which are the responsible parameters of the overall magnitude, should be rather unaffected by the discussed approximation. Hence, since these parameters are the only ones which explicitly contain the Berry curvature, we argue that our main conclusion regarding the strength of the Berry curvature is still valid despite the fact that the temperature fit of the Hall coefficient is not as good as that for the Peltier coefficient.

APPENDIX C: LOW-FIELD NERNST SIGNAL AND MAGNETIZATION BEHAVIOR

In addition to the discussed findings of the main text we would like to mention the low-field region of the Nernst data. As highlighted in Fig. 9, both the S_{xz} versus B and the S_{yz} versus B curves (the latter are not shown) exhibit a hysteresis cycle which remains almost unaltered from 5 K up to room temperature. This cycle is rectangular-shaped and closes at around 20 mT, in agreement with the previous report on Mn_3Sn [17]. Remarkably, the cycle exhibits a total extension of around $\Delta S_{xz} = 2\,\mu$V/K at 100 K (even overcoming the

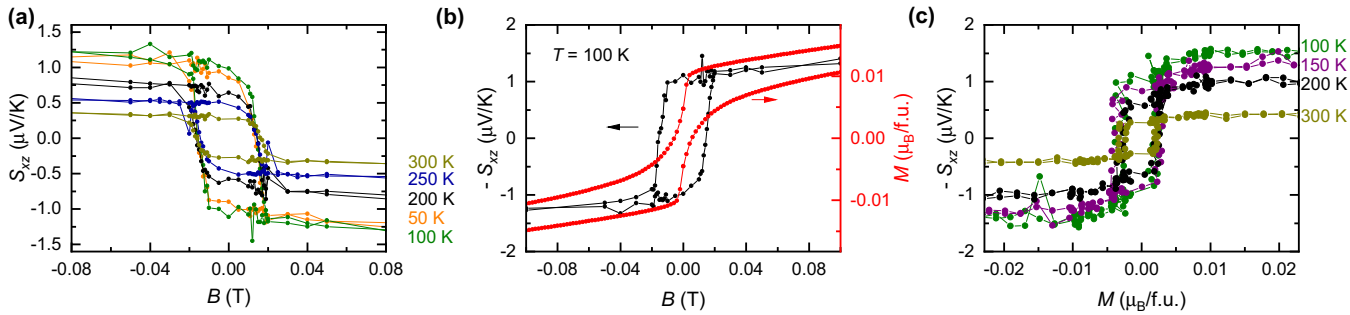

FIG. 9. (a) Zoom-in of $S_{xz}(B)$ with a clearly visible hysteresis of the Nernst signal at different selected temperatures. (b) Comparison of the hysteresis curves of $S_{xz}(B)$ and the magnetization M in the y direction at $T = 100$ K. B denotes the external magnetic field. (c) S_{xz} vs M. There is no obvious scaling of the anomalous Nernst signal on the magnetization of the sample.

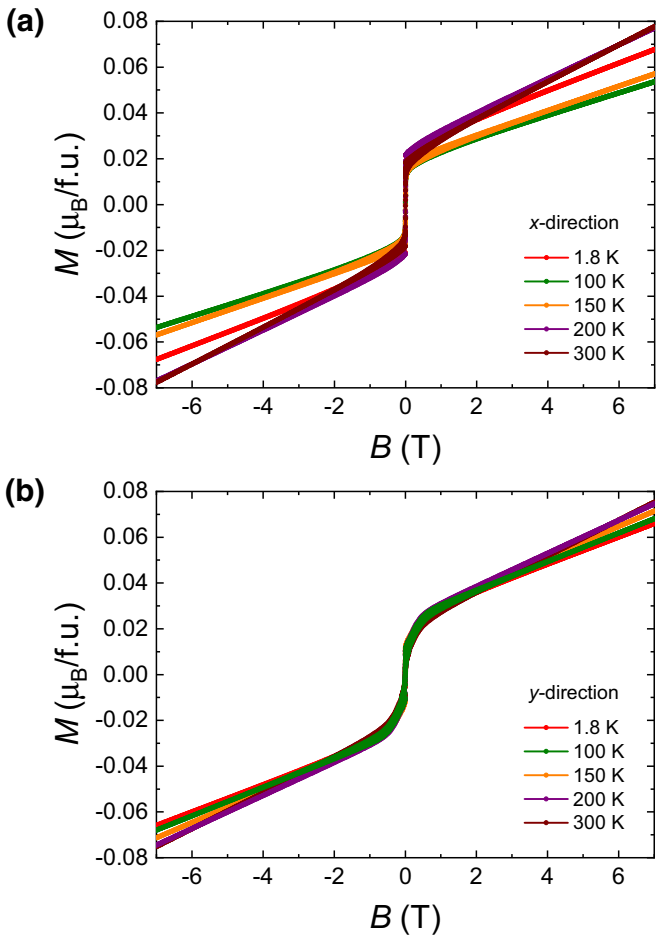

FIG. 10. Magnetic moment of Mn_3Ge in the (a) x direction and (b) y direction. The magnetization has been corrected for geometry effects. However, demagnetization corrections are small and have not been applied. B denotes the external magnetic field.

peak value of $\Delta S_{xz} = 0.7\,\mu$V/K observed in Mn_3Sn [17]) with negligible net magnetization. This exceptionally large value underpins that noncollinear antiferromagnets such as Mn_3Ge and Mn_3Sn may constitute a new material paradigm in the field of spintronic [3,5,35–37] and thermoelectric technologies [17,38].

It is interesting to compare this low-field behavior of the ANE with the DC magnetization. The latter was measured as a function of the temperature and magnetic field by means of a quantum interference device magnetometer (SQUID-VSM) by Quantum Design. For the purpose of a direct comparison with the Nernst effect measurements, the magnetization curves were obtained by applying an external magnetic field in the direction(s) [2-1-10] (and [01-10]). In order to probe the field-dependent magnetization, M(B) (Fig. 9) was measured upon sweeping the magnetic field between -7 T and 7 T at constant temperatures 1.8, 50, 100, 150, 200, 250, and 300 K. Given the large magnitude of the measured magnetic signal, the small background correction due to the diamagnetic contribution of the glue GE-Varnish used to fix the sample has been neglected.

It is well known that a magnetization (even for a relatively small value) may enhance the ANE as is the case in ferromagnets where the anomalous Hall conductivity is usually assumed to be proportional to the magnetization of the magnetic material. Interestingly, such a proportionality between the ANE and the magnetization M is absent in Mn_3Ge [see Fig. 10(b)]. Even if M somehow reproduces the overall hysteresis shape in the low field region it closes the cycle at much higher fields with respect to S_{xz}. Furthermore, while S_{xz} is anomalous and as such stays constant with increasing B, M undergoes an almost linear drift. We also verified the absence of a scaling of the two quantities by plotting S_{xz} versus M in Fig. 10(c).

[1] X. Wan, A. M. Turner, A. Vishwanath, and S. Y. Savrasov, Phys. Rev. B **83**, 205101 (2011).

[2] L. X. Yang, Z. K. Liu, Y. Sun, H. Peng, H. F. Yang, T. Zhang, B. Zhou, Y. Zhang, Y. F. Guo, M. Rahn, D. Prabhakaran, Z. Hussain, S.-K. Mo, C. Felser, B. Yan, and Y. L. Chen, Nat. Phys. **11**, 728 (2015).

[3] S. Nakatsuji, N. Kiyohara, and T. Higo, Nature (London) **527**, 212 (2015).

[4] N. P. Armitage, E. J. Mele, and A. Vishwanath, Rev. Mod. Phys. **90**, 015001 (2018).

[5] M. Kimata, H. Chen, K. Kondou, S. Sugimoto, P. K. Muduli, M. Ikhlas, Y. Omori, T. Tomita, A. H. MacDonald, S. Nakatsuji, and Y. Otani, Nature (London) **565**, 627(2019).

[6] H. Kurebayashi, J. Sinova, D. Fang, A. C. Irvine, T. D. Skinner, J. Wunderlich, V. Novák, R. P. Campion, B. L. Gallagher, E. K. Vehstedt, L. P. Zârbo, K. Výborný, A. J. Ferguson, and T. Jungwirth, Nat. Nanotech. **9**, 211 (2014).

[7] C. G. Yale, F. J. Heremans, B. B. Zhou, A. Auer, G. Burkard, and D. D. Awschalom, Nat. Photon. **10**, 184 (2016).

[8] D. Xiao, M.-C. Chang, and Q. Niu, Rev. Mod. Phys. **82**, 1959 (2010).

[9] G. Sundaram and Q. Niu, Phys. Rev. B **59**, 14915 (1999).

[10] N. Nagaosa, J. Sinova, S. Onoda, A. H. MacDonald, and N. P. Ong, Rev. Mod. Phys. **82**, 1539 (2010).

[11] J. Noky, J. Gayles, C. Felser, and Y. Sun, Phys. Rev. B **97**, 220405(R) (2018).

[12] F. Caglieris, C. Wuttke, S. Sykora, V. Süss, C. Shekhar, C. Felser, B. Büchner, and C. Hess, Phys. Rev. B **98**, 201107(R) (2018).

[13] S. J. Watzman, T. M. McCormick, C. Shekhar, S.-C. Wu, Y. Sun, A. Prakash, C. Felser, N. Trivedi, and J. P. Heremans, Phys. Rev. B **97**, 161404(R) (2018).

[14] A. Sakai, Y. P. Mizuta, A. A. Nugroho, R. Sihombing, T. Koretsune, M.-T. Suzuki, N. Takemori, R. Ishii, D. Nishio-Hamane, R. Arita, P. Goswami, and S. Nakatsuji, Nat. Phys. **14**, 1119 (2018).

[15] X. Li, L. Xu, L. Ding, J. Wang, M. Shen, X. Lu, Z. Zhu, and K. Behnia, Phys. Rev. Lett. **119**, 056601 (2017).

[16] A. K. Nayak, J. E. Fischer, Y. Sun, B. Yan, J. Karel, A. C. Komarek, C. Shekhar, N. Kumar, W. Schnelle, J. Kübler, C. Felser, and S. S. P. Parkin, Sci. Adv. **2**, e1501870 (2016).

[17] M. Ikhlas, T. Tomita, T. Koretsune, M.-T. Suzuki, D. Nishio-Hamane, R. Arita, Y. Otani, and S. Nakatsuji, Nat. Phys. **13**, 1085 (2017).

[18] H. Chen, Q. Niu, and A. H. MacDonald, Phys. Rev. Lett. **112**, 017205 (2014).
[19] G.-Y. Guo and T.-C. Wang, Phys. Rev. B **96**, 224415 (2017).
[20] P. J. Brown, V. Nunez, F. Tasset, J. B. Forsyth, and P. Radhakrishna, J. Phys.: Condens. Matter **2**, 9409 (1990).
[21] W. J. Feng, D. Li, W. J. Ren, Y. B. Li, W. F. Li, J. Li, Y. Q. Zhang, and Z. D. Zhang, Phys. Rev. B **73**, 205105 (2006).
[22] J. F. Qian, A. K. Nayak, G. Kreiner, W. Schnelle, and C. Felser, J. Phys. D **47**, 305001 (2014).
[23] N. Yamada, H. Sakai, H. Mori, and T. Ohoyama, Physica B+C **149**, 311 (1988).
[24] S. Tomiyoshi and Y. Yamaguchi, J. Phys. Soc. Jpn. **51**, 2478 (1982).
[25] T. Nagamiya, S. Tomiyoshi, and Y. Yamaguchi, Solid State Commun. **42**, 385 (1982).
[26] H. Yang, Y. Sun, Y. Zhang, W.-J. Shi, S. S. P. Parkin, and B. Yan, New J. Phys. **19**, 015008 (2017).
[27] S. Tomiyoshi, Y. Yamaguchi, and T. Nagamiya, J. Magn. Magn. Mater. **31-34**, 629 (1983).
[28] Upon finalizing this manuscript we became aware of the research of Ref. [34]. The Nernst data are in good agreement with our measurement; however, only one configuration of S_{ij} was measured, and the focus is lying on the relations between different transverse transport coefficients such as the Wiedemann-Franz law. The calculated SOC-induced gap that this work is showing does not influence our argument.
[29] For simplicity, a special index for highlighting those coefficients as anomalous is omitted in the following.
[30] M. Meinero, F. Caglieris, G. Lamura, I. Pallecchi, A. Jost, U. Zeitler, S. Ishida, H. Eisaki, and M. Putti, Phys. Rev. B **98**, 155116 (2018).
[31] L. Xu, X. Li, X. Lu, C. Collignon, H. Fu, B. Fauqué, B. Yan, Z. Zhu, and K. Behnia, arXiv:1812.04339.
[32] G. Sharma, P. Goswami, and S. Tewari, Phys. Rev. B **93**, 035116 (2016).
[33] R. Kubo, J. Phys. Soc. Jpn. **12**, 570 (1957).
[34] L. Xu, X. Li, X. Lu, C. Collignon, H. Fu, B. Fauque, B. Yan, Z. Zhu, and K. Behnia, arXiv:1812.04339 (2018).
[35] A. K. Nayak, M. Nicklas, S. Chadov, P. Khuntia, C. Shekhar, A. Kalache, M. Baenitz, Y. Skourski, V. K. Guduru, A. Puri, U. Zeitler, J. M. D. Coey, and C. Felser, Nat. Mater. **14**, 679 (2015).
[36] B. G. Park, J. Wunderlich, X. Martí, V. Holý, Y. Kurosaki, M. Yamada, H. Yamamoto, A. Nishide, J. Hayakawa, H. Takahashi, A. B. Shick, and T. Jungwirth, Nat. Mater. **10**, 347 (2011).
[37] X. Marti, I. Fina, C. Frontera, J. Liu, P. Wadley, Q. He, R. J. Paull, J. D. Clarkson, J. Kudrnovský, I. Turek, J. Kuneš, D. Yi, J.-H. Chu, C. T. Nelson, L. You, E. Arenholz, S. Salahuddin, J. Fontcuberta, T. Jungwirth, and R. Ramesh, Nat. Mater. **13**, 367 (2014).
[38] S. Mizukami, A. Sakuma, A. Sugihara, T. Kubota, Y. Kondo, H. Tsuchiura, and T. Miyazaki, Appl. Phys. Expr. **6**, 123002 (2013).